

Excitons and polaritons in planar heterostructures in external electric and magnetic fields: A multi-sub-level approach



J. Wilkes^{*}, E.A. Muljarov

School of Physics and Astronomy, Cardiff University, The Parade, Cardiff CF24 3AA, United Kingdom

ARTICLE INFO

Article history:

Received 14 November 2016

Received in revised form 10 January 2017

Accepted 16 January 2017

Available online 18 January 2017

Keywords:

Coupled quantum wells

Microcavity polariton

Indirect exciton

Dipolariton

ABSTRACT

Excitons and microcavity polaritons that possess a macroscopic dipole alignment are attractive systems to study. This is due to an enhancement of collective many body effects and an ability to electrostatically control their transport and internal structure. Here, we present an overview of a rigorous calculation of spatially-indirect exciton states in semiconductor coupled quantum wells in externally applied electric and magnetic fields. We also treat dipolaritons that form when such structures are positioned at the antinode of a resonant cavity mode. Our approach is general and can be applied to various planar solid state heterostructures inside optical resonators. It offers a thorough description of the properties of excitons and polaritons that are important for modelling their respective fluids. In particular, we calculate the exciton Bohr radius, binding energy, optical lifetime and magnetic field induced enhancement of the effective mass. We also describe electric and magnetic field control of the exciton and polariton dipole moment and brightness.

© 2017 The Authors. Published by Elsevier Ltd. This is an open access article under the CC BY license (<http://creativecommons.org/licenses/by/4.0/>).

Contents

1. Introduction	33
2. Microscopic model of CQW excitons in applied electric and magnetic fields	33
2.1. Exciton Schrödinger equation	33
2.2. Solution of the exciton Schrödinger equation using the MSLA	35
3. Application to symmetric GaAs/AlGaAs CQWs	35
3.1. Exciton absorption spectrum	35
3.2. Electric field driven direct-indirect exciton crossover	36
3.3. Magnetic field induced exciton effective mass enhancement	36
3.4. Optical lifetime of exciton fluids	37
4. Polaritons in microcavity embedded CQWs in externally applied fields	38
4.1. Coupled Maxwell's and material equations	38
4.2. Field dependence of the polariton reflectivity spectrum	39
4.3. Brightness and dipole moment of the polariton branches	39
5. Summary	40
Acknowledgements	40
References	40

^{*} Corresponding author.

E-mail address: WilkesJ1@cf.ac.uk (J. Wilkes).

1. Introduction

An exciton is a hydrogen-like bound state of an electron and a hole and can be realized via photoexcitation of semiconductor quantum wells (QWs). QW excitons were studied intensively for the observation of Bose-Einstein condensation (BEC) [1]. To that end, a key benefit of using excitons is that the critical temperature of BEC is orders of magnitude higher compared to the atomic gases for which BEC was first reported [2]. In a pair of electronically coupled QWs (CQWs), one may have direct excitons, formed from an electron and a hole in the same QW, and indirect excitons, formed from an electron and a hole in adjacent QWs. The latter becomes the ground state of the system when an electric field is applied parallel to the heterostructure growth axis. Due to the macroscopic charge separation, indirect excitons acquire a static dipole moment. This causes strong dipolar interactions between excitons which can be probed via a density dependent blue shift of the emission line [3,4]. It results in excitons screening the QW disorder potential, allowing exciton transport over tens of micrometers. Further, the indirect exciton energy decreases with increasing electric field. Spatial modulation of the applied field can therefore be used to create potential landscapes for excitons and provides a means to control their transport [5–7]. This was exploited for the creation of exciton mediated optical devices [8]. The reduced overlap of electron and hole wave functions extends the lifetime of indirect excitons by orders of magnitude compared to direct excitons. This allows long range transport, buildup of high densities and cooling below the onset of quantum degeneracy within their lifetime. Such a combination makes indirect excitons ideal for studying quantum many-body effects in cold composite bosons in a solid state system.

Exciton-polaritons (or simply polaritons) are a mixed state of a QW exciton and the resonant mode of a microcavity in the strong light-matter coupling regime. They are formed when QWs are placed between two distributed Bragg reflectors (DBRs) at the anti-node positions of a resonant mode of the optical microcavity. The polariton effective mass is smaller than that of the exciton and is mainly determined by the cavity photon mass. Exciton-polaritons have proven to be among the best tools to study the beauty of quantum mechanics. They exhibit striking features such as condensation [9], superfluidity [10] and the formation of quantum vortices [11]. Polaritons can acquire the dipole moment of an indirect exciton when CQWs are embedded in the microcavity. Although the indirect exciton is only weakly coupled to light, it is electronically coupled to the bright direct exciton. Then, an effective three-level system composed of a cavity photon, a bright direct and a dark indirect exciton is formed, producing mixed states. These mixed states are known as dipolar polaritons, or dipolaritons [12]. Similar to indirect excitons, the dipolar interactions are significantly stronger compared to those of regular polaritons and are observable via a density-dependent blue shift of the dipolariton emission line [13]. Long dipolariton lifetimes are possible using high quality microcavities. Recently, lifetimes of a few hundred pico seconds were achieved for polaritons in single QWs [14,40]. Dipolaritons therefore present the prospect to combine all the most useful features of indirect excitons with a stronger light-matter coupling and a higher condensation temperature. This renders them ideal for the observation and control of quantum phenomena on a macroscopic scale. On offer is a greater flexibility of control and new possible applications compared to regular polaritons formed from direct excitons. Proposed applications include THz emission [15,16], tunable single-photon emission [17], optical parametric oscillators [18], quantum logic gates [19], and the creation of condensates of indirect excitons [20] and dipolaritons [21].

A detailed microscopic model of excitons and polaritons is important for understanding and predicting the physical properties of the systems described above. In this paper, we overview a multi-sub-level approach (MSLA) to solving the exciton Schrödinger equation in real space in three dimensions (3D). This approach was recently developed to describe indirect excitons in CQWs [22]. In particular, a full description of carrier tunnelling and the electric field driven direct-to-indirect exciton crossover was provided. The MSLA was used to investigate the internal structure of exciton states and to calculate the exciton absorption spectrum as a function of electric field [22,23] and heterostructure dimensions [24]. The dependence of the properties of excitons on an applied magnetic field, including the magnetic field induced effective mass enhancement were also calculated [25]. By combining with the scattering matrix method [26], the MSLA was used to describe strong coupling of excitons with cavity photons [27]. With the inclusion of an applied magnetic field, magneto-dipolariton states were calculated [28].

The exciton Schrödinger problem and details of the MSLA are described in Section 2. Results of a study of a commonly used GaAs symmetric CQW heterostructure are given in Section 3. The numerical method of solving the coupled Maxwell and Schrödinger equations for dipolaritons is outlined in Section 4, with an illustration on an asymmetric InGaAs microcavity embedded CQW. Section 5 provides a summary of our findings.

2. Microscopic model of CQW excitons in applied electric and magnetic fields

2.1. Exciton Schrödinger equation

In semiconductor QWs with external bias and magnetic field orientated normal to the QW plane, the wave function of an exciton with finite in-plane momentum \mathbf{P} can be written in the variable-separable form [29,30],

$$\Psi(\mathbf{r}_e, \mathbf{r}_h) = \exp\left(i\left[\mathbf{P} + \frac{e}{c}\mathbf{A}(\boldsymbol{\rho})\right] \cdot \frac{\mathbf{R}}{\hbar}\right) e^{im\theta} \varphi(\rho, z_e, z_h). \quad (1)$$

Here, $\mathbf{r}_{e(h)}$, is the 3D electron (hole) coordinate, \mathbf{R} and $\boldsymbol{\rho} = (\rho, \theta)$ are the 2D in-plane center of mass (COM) and relative coordinates, respectively, and $\mathbf{A}(\mathbf{r}) = \mathbf{B} \times \mathbf{r}/2$ is the magnetic vector potential using the symmetric gauge. As the exciton COM moves in the perpendicular magnetic field, the electron and hole each experience the Lorentz force, equal in magnitude but opposite in direction. The magnetic field therefore couples the COM and internal degrees of freedom. The first exponential factor in (1) describes this coupling and the COM motion itself. The second exponential factor describes the exciton angular momentum with magnetic quantum number m and angular coordinate θ . Finally, the wave function $\varphi(\rho, z_e, z_h)$ describes the electron-hole relative motion with $\rho = |\boldsymbol{\rho}|$ and $z_{e(h)}$ the electron (hole) coordinate along the growth axis. It is an eigen state of the Hamiltonian describing the internal structure of an exciton with $\mathbf{P} = 0$, derived in Ref. [25]:

$$\hat{H}_x^0(\rho, z_e, z_h) = \hat{H}_e^\perp(z_e) + \hat{H}_h^\perp(z_h) + \hat{K}(\rho) + V_B(\rho) - \frac{e^2}{\epsilon_b \sqrt{\rho^2 + (z_e - z_h)^2}} + E_g. \quad (2)$$

The Hamiltonians of the electron and hole perpendicular motion are

$$\hat{H}_{e,h}^\perp(z) = -\frac{\hbar^2}{2} \frac{\partial}{\partial z} \frac{1}{m_{e,h}^\perp(z)} \frac{\partial}{\partial z} + U_{e,h}(z). \quad (3)$$

These describe the Coulomb-uncorrelated single particle electron and hole states in CQWs in the absence of a magnetic field. They are characterized by the effective masses $m_{e,h}^\perp(z)$ along the growth axis and the potentials due to the applied electric field and QW confinement, embodied in $U_{e,h}(z)$. The Schrödinger equations $\hat{H}_{e,h}^\perp \psi_q^{e,h} = E_q^{e,h} \psi_q^{e,h}$ are solved numerically to obtain the wave functions $\psi_q^{e,h}(z)$, where the index q labels the electron (hole) states quantized in the CQW heterostructure potentials. Fig. 1(a) shows the electron band structure along the growth axis of an exemplar CQW heterostructure that was studied in Ref. [12]. The left and right $\text{In}_x\text{Ga}_{1-x}\text{As}$ 10 nm thick QWs have $x = 0.08$ and $x = 0.1$, respectively, and are separated by a 4 nm GaAs barrier. The confinement potentials are tilted by the perpendicular electric field, $F = 15$ kV/cm. The single particle wave functions of the first two electron ($e1, e2$) and first three hole ($h1, h2, h3$) states are also shown, each offset by their energy.

At high electric field, tilting of the CQW confinement potential spatially separates the electron and hole ground states ($e1$ and $h1$). The exciton thus acquires a large dipole moment that is comparable to the nominal center-to-center distance between the QWs. The electric field dependence of the electron and hole energies are shown in Fig. 1(b) and (c), respectively. For electrons, one can see that the QW asymmetry is partly compensated at around 12 kV/cm, forming resonantly tunnel coupled symmetric and antisymmetric states. A similar effect takes place around 6 kV/cm for the hole when the ground state in the left QW is resonantly coupled to the first excited state in the right QW. Away from the tunnelling resonance, the derivative of the energy of each single particle state with respect to electric field is approximately equal to the product of charge and the expectation value of the particle's position, $\pm e\langle z \rangle$.

The kinetic term in (2), $\hat{K}(\rho)$, is given by

$$\hat{K}(\rho) = -\frac{\hbar^2}{2\mu} \left[\frac{\partial^2}{\partial \rho^2} + \frac{1}{\rho} \frac{\partial}{\partial \rho} - \frac{m^2}{\rho^2} \right], \quad (4)$$

where $\mu = (1/m_e^\parallel + 1/m_h^\parallel)^{-1}$ is the in-plane reduced exciton mass. The potential due to the magnetic field is

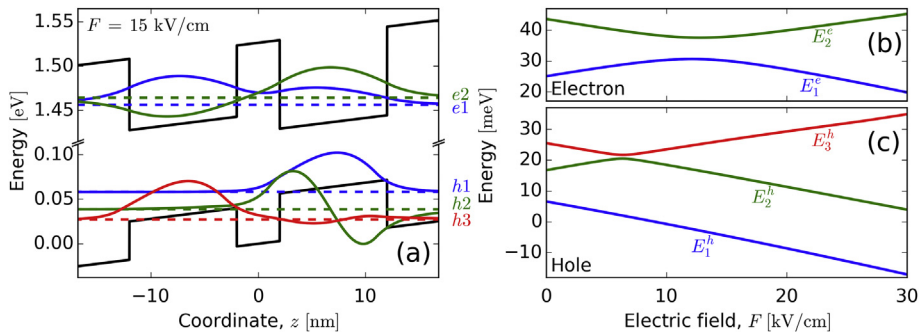


Fig. 1. (a) Electron band structure and first few electron ($e1$ and $e2$) and hole ($h1, h2$ and $h3$) states for $F = 15$ kV/cm in 10–4–10-nm InGaAs asymmetric CQWs used in Ref. [12]. (b) Electron and (c) hole energy levels as functions of electric field.

$$V_B(\rho) = \frac{e\hbar mB}{2\kappa c} + \frac{e^2 B^2 \rho^2}{8\mu\epsilon^2}, \quad (5)$$

where $\kappa = (1/m_e^\parallel - 1/m_h^\parallel)^{-1}$ is the magnetic dipole mass [31]. The first term appears due to the exciton magnetic dipole and its interaction with the magnetic field. The second term describes the diamagnetic shift. The last two terms in (2) are the electron-hole Coulomb interaction and band gap energy. ϵ_b is the background permittivity in the QW layers.

2.2. Solution of the exciton Schrödinger equation using the MSLA

We solve the Schrödinger equation $\hat{H}_x^0 |v, m\rangle = E_{v,m} |v, m\rangle$ where $|v, m\rangle$ is the v -th quantized exciton state in a CQW in finite electric and magnetic fields with magnetic quantum number m and eigen energy $E_{v,m}$. The solution is obtained numerically using the MSLA developed in Refs. [22,25]. The foundation of this method is to expand the exciton relative motion wave function into the set of Coulomb uncorrelated electron-hole pair states,

$$\varphi_{v,m}(\rho, z_e, z_h) = \sum_{n=1}^{N_e N_h} \Phi_n(z_e, z_h) \phi_n^{v,m}(\rho). \quad (6)$$

Here, $\Phi_n(z_e, z_h) = \psi_{p_n}^e(z_e) \psi_{q_n}^h(z_h)$ are the set of orthogonal basis states given by the product of electron and hole single-particle states, shown in Fig. 1(a). The index n counts over all basis states and $n \mapsto (p_n, q_n)$ maps the pair index n onto the indices of electron and hole quantized states. The number of basis states obtained from N_e electron states and N_h hole states is $N_e N_h$.

The radial components of the wave function $\phi_n^{v,m}(\rho)$ are calculated using the shooting method. This involves integrating the Schrödinger equation from large ρ down to $\rho = 0$, using the boundary conditions following from large and small ρ asymptotics of the wave function. The numerical solution is generated on a logarithmic grid and we use fourth-order linear multistep Numerov's algorithm for the finite difference approximations of the derivatives. For a wave function of the form (6) with $N_e N_h$ components, this requires a matrix generalization of Numerov's method, which has been successfully developed for the MSLA [25].

3. Application to symmetric GaAs/AlGaAs CQWs

Here, we illustrate the MSLA applying it to a planar heterostructure. As an example, we consider 8-4-8 nm GaAs/Al_{0.33}Ga_{0.67}As symmetric CQWs that were studied in Refs. [32–34].

3.1. Exciton absorption spectrum

States with zero angular momentum have radiative lifetime given by the overlap integral of electron and hole wave functions,

$$\frac{1}{\tau_R^{(v)}} = \frac{2\pi e^2 |d_{cv}|^2 E_{v,0}}{\hbar c \sqrt{\epsilon_b}} \left| \sum_{n=1}^{N_e N_h} \phi_n^{v,0}(0) \int \Phi_n(z, z) dz \right|^2. \quad (7)$$

Here, d_{cv} is the dipole matrix element between the conduction and valence bands. From the linewidth of the optical transition $\Gamma_v = 1/\tau_R^{(v)}$, we use the Lorentzian model of absorbing oscillators to calculate the exciton absorption spectrum. This is shown in Fig. 2 as a function of electric and magnetic field. Fig. 2(a) shows the electric field dependence with a magnetic field

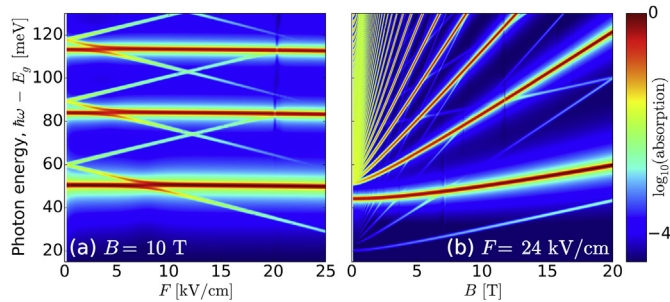


Fig. 2. (a) Electric field dependence of the exciton absorption spectrum in 10 T magnetic field. (b) Magnetic field dependence of the exciton absorption spectrum in 24 kV/cm electric field.

$B = 10$ T. The three brightest lines whose energy is almost independent of electric field are due to the lowest three Landau levels of direct excitons. Each of these lines consists of two absorption peaks originating from direct excitons in left and right QWs that are very close in energy. The weaker absorption lines originate from dark indirect excitons. With increasing electric field, these states either decrease or increase in energy depending on whether their static dipole moment is aligned with or against the electric field. Similar to direct excitons, the first three Landau levels of each orientation of indirect excitons are seen. The Landau fans of bright direct and dark indirect excitons in a magnetic field are shown in Fig. 2(b) for electric field $F = 24$ kV/cm.

3.2. Electric field driven direct-indirect exciton crossover

Calculation of the wave functions that describe the exciton's internal structure allows to determine a number of observables. Fig. 3 shows the electric field dependence of the properties of the exciton ground state for different values of magnetic field. As the electric field is increased from zero to 10 kV/cm, the ground state undergoes a crossover from a direct to an indirect exciton. This is characterized by an increase in the dipole moment $|\langle z_e - z_h \rangle|$ of about 12 nm which corresponds to the center-to-center distance of the QWs (see Fig. 3(a)). The increased spatial separation of the electron and the hole weakens their mutual Coulomb interaction. This results in an increase in the in-plane Bohr radius $r_B = \sqrt{\langle \rho^2 \rangle}$ (Fig. 3(b)) and a decrease in the exciton binding energy (Fig. 3(c)). Due to the decrease in the electron-hole overlap integral (7) the radiative lifetime $\tau_R = \tau_R^{(0)}$ increases by a few orders of magnitude (Fig. 3(d)).

The application of a perpendicular magnetic field suppresses the electric field driven direct-indirect exciton crossover. This effect originates from tightening of the electron and hole cyclotron orbits that enters the model via the parabolic potential in (5). The magnetic field therefore acts to shrink the in-plane Bohr radius. This enhances the electron-hole Coulomb interaction and, in turn, makes a direct exciton more energetically favourable to higher electric fields. This is made explicit in the inset in Fig. 3(a). We define the direct-indirect crossover point F_c as the value of electric field where the dipole moment is equal to half the center-to-center distance of the QWs and show F_c as a function of magnetic field. In addition to increasing F_c , the magnetic field induced shrinkage of the in-plane component of the exciton wave function causes a shortening of the exciton lifetime and an enhancement of the binding energy.

3.3. Magnetic field induced exciton effective mass enhancement

Magnetoexcitons with non-zero in-plane COM momentum \mathbf{P} consist of an electron and a hole that experience the Lorentz force in opposite directions. This acts to separate the pair and is balanced by the Coulomb force that they exert on each other. The Lorentz force increases with increasing \mathbf{P} . Effectively, this stretches the electron-hole bond, raising the eigen energy of the magnetoexciton, owing to the change of its internal structure. This additional energy cost associated with the magnetoexciton COM motion is manifested as an inertia. For an exciton with a finite in-plane COM momentum $\mathbf{P} \neq 0$, the Hamiltonian (2) is modified to [25],

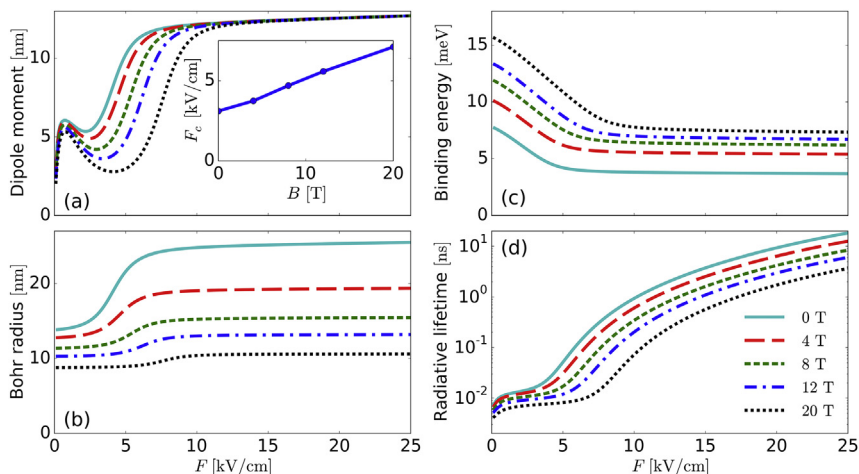


Fig. 3. Electric field dependence of the magnetoexciton ground state. (a) Perpendicular dipole length, (b) in-plane Bohr radius, (c) binding energy, and (d) radiative lifetime. The inset in (a) shows the magnetic field dependence of the direct-indirect exciton crossover point, defined as the electric field where the dipole moment is half the QW center-to-center distance.

$$\hat{H}_x^{\mathbf{P}} = \hat{H}_x^0 + \frac{P^2}{2M_x} + \frac{2e}{M_x c} \mathbf{P} \cdot \mathbf{A}(\rho), \quad (8)$$

with $P = |\mathbf{P}|$ and M_x being the in-plane exciton mass in the absence of magnetic field. For small \mathbf{P} and any magnetic field B , the magnetoexciton has parabolic dispersion and can be described by an effective mass. Treating P as a small parameter and using perturbation theory up to second order, we derive the exciton effective mass renormalization due to the magnetic field as

$$\frac{1}{M_x^*} = \frac{1}{M_x} + 2 \left(\frac{2e}{M_x c P} \right)^2 \sum_{\substack{j \neq \nu \\ m = \pm 1}} \frac{|\langle \nu, 0 | \mathbf{P} \cdot \mathbf{A}(\rho) | j, m \rangle|^2}{E_{\nu,0} - E_{j,m}}. \quad (9)$$

Here, the index j counts over the eigenstates with the angular momenta $m = \pm 1$ which contribute in 2nd order and which are calculated at given values of electric and magnetic field. Fig. 4 shows the effective mass enhancement of the exciton ground state calculated for symmetric GaAs/AlGaAs CQWs. For small electric fields ($F = 3$ kV/cm), the ground state is a tightly bound direct exciton (see Fig. 3) which is not easily perturbed by the Lorentz force. The corresponding mass enhancement is therefore rather slow. In contrast, a weakly bound indirect exciton that exists in the high electric field limit ($F = 24$ kV/cm) is strongly perturbed by the Lorentz force and has a significant enhancement of the effective mass. In between these two limits, the magnetic field induces a crossover of the ground state from being indirect to direct. This crossover is the cause of the non-monotonous behaviour of the exciton effective mass at intermediate electric fields. As the magnetic field increases, the ground state smoothly transforms from an indirect to a direct exciton and the effective mass shifts its trend accordingly, from a steep rate of change to a shallower one.

The advantage of our approach compared to some previous calculations of the exciton mass renormalization is that the perturbation is in P only, allowing the B -field to be arbitrarily large. In contrast, the approach developed in Ref. [35] used the magnetic field as a small parameter of the perturbation theory. Consequently, the applicability of the latter is restricted to low magnetic field (up to ≈ 2 T in the structure considered in that paper). Another significant benefit of our approach is that the full 3D solution of the exciton Schrödinger equation (2) describes the inter-well coupling that is neglected by any 2D approximation [31,35].

3.4. Optical lifetime of exciton fluids

In experiments, the optical lifetime of an exciton gas can be directly measured from the decay in emission intensity over time that follows termination of an excitation beam [36]. To make a suitable comparison with such experiments, the thermal distribution of excitons needs to be considered. In particular, only excitons inside the *radiative zone* can recombine to emit light. This is a region in momentum space that is contained within the intersection between the exciton and photon dispersion surfaces. We account for the occupation of the radiative zone by an equilibrium Bose gas and the photon density of states using the following form for the optical lifetime [37],

$$\frac{1}{\tau_{\text{opt}}} = \frac{1}{2\tau_R} \frac{E_\gamma}{k_B T_0} \int_0^1 \frac{1 + u^2}{(e^{E_\gamma(1-u^2)/k_B T}) / (1 - e^{-T_0/T}) - 1} du. \quad (10)$$

Here, $E_\gamma = \hbar^2 k_\gamma^2 / 2M^*$ where k_γ marks the intersection of the exciton and photon dispersions and satisfies the equation $E_{0,0} + E_\gamma = \hbar c k_\gamma / \sqrt{\epsilon_b}$. Electric and magnetic field dependence of E_γ enters via the $P = 0$ energy $E_{0,0}$ and effective mass M^* of

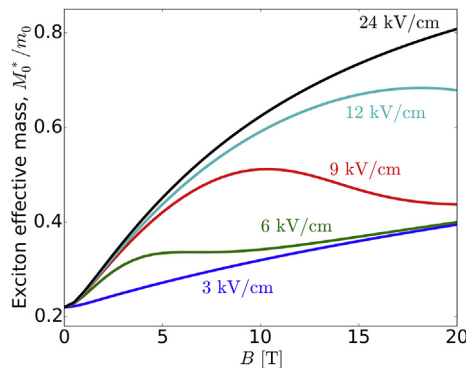


Fig. 4. Electric and magnetic field dependence of the exciton ground state renormalized effective mass.

the exciton ground state. T and $T_0 = (\pi\hbar^2 n_x)/(2M^*k_B)$ are the temperature and quantum degeneracy temperature of the exciton gas. In the latter, n_x is the 2D density of excitons. τ_R is the electric and magnetic field dependent single exciton radiative lifetime, as described above. The additional prefactor of 1/2 in (10) includes the fact that only two out of the four spin degenerate exciton states are optically active. Exciton states with the z -projection of the total spin ± 1 are optically active while those with spin ± 2 are dark. An even distribution over spin states is justified when their energy splitting is small compared to the thermal energy, which is typical for the structures considered here [38]. Fig. 5(a) shows the calculation of the exciton effective mass and the corresponding value of E_γ for $F = 30$ kV/cm. The mass enhancement reduces the size of the radiative zone leading to suppression of the optical decay of the exciton gas. Fig. 5(b) shows the optical lifetime, calculated using (10) for different temperatures and an exciton density $n_x = 5 \times 10^{10}$ cm $^{-2}$. At temperatures below 1 K, the lifetime closely follows that of single excitons (multiplied by two, due to the distribution among bright and dark states). At higher temperatures the lifetime is enhanced as a smaller fraction of excitons have momentum inside the radiative zone. Moreover, the trend of τ_{opt} changes from decreasing to increasing with magnetic field. An enhancement of the exciton lifetime with increasing magnetic field is consistent with experimental observations [36].

4. Polaritons in microcavity embedded CQWs in externally applied fields

4.1. Coupled Maxwell's and material equations

The exciton states calculated in Section 2.2 can be used to calculate polariton states that are present in CQWs embedded in an optical microcavity which is formed from a pair of distributed Bragg reflectors (DBRs). We consider the asymmetric CQW structures shown in Fig. 1(a) and solve Maxwell's wave equation for the light field $\mathcal{E}(z)$, which takes the form

$$\left(\frac{p^2}{\hbar^2} - \frac{\partial^2}{\partial z^2}\right) \mathcal{E}(z) = \frac{\omega^2}{c^2} \left[\epsilon_b(z) \mathcal{E}(z) + 4\pi \int \chi(z, z') \mathcal{E}(z') dz' \right], \quad (11)$$

where ω is the frequency of light. The wave vector, P/\hbar is equal to that of the exciton due to conservation of momentum in the plane of the QW. The permittivity along the z -axis of the microcavity $\epsilon_b(z)$ considered here is shown in Fig. 6(a). The structure consists of 17 and 21 pairs of alternating GaAs and InGaAs $\lambda/4$ layers forming the DBRs with four pairs of asymmetric CQWs placed at the antinode positions of the resonant optical mode in a $5\lambda/2$ cavity. The excitonic susceptibility $\chi(z, z')$ is found by solving an inhomogeneous Schrödinger equation [39]. This is done using the Green's function approach [28] which gives $\chi(z, z')$ as a sum over all quantized exciton states:

$$\chi(z, z') = e^2 d_{\text{cv}}^2 \hbar \omega \sum_{\nu} \frac{\varphi_{\nu 0 \mathbf{P}}(0, z, z) \varphi_{\nu 0 \mathbf{P}}(0, z', z')}{(E_{\nu 0 \mathbf{P}} - i\gamma)(E_{\nu 0 \mathbf{P}} - i\gamma - \hbar\omega)}. \quad (12)$$

Here, γ is a phenomenological damping constant and we added the extra index on $\varphi_{\nu 0 \mathbf{P}}$ and $E_{\nu 0 \mathbf{P}}$ to denote the in-plane momentum.

The reflectivity spectrum of the cavity without CQWs ($\chi = 0$) is shown in Fig. 6(b). A dip in reflectivity occurs at the cavity mode, shown in detail by the inset in Fig. 6(b). The cavity mode has a full width at half-maximum of 0.1 meV giving a Q-factor of ≈ 14000 . An example of the full reflectivity spectrum including the light-matter interaction in the CQWs is shown by the grayscale in Fig. 6(c) as a function of in-plane wave vector for $F = 20$ kV/cm and $B = 10$ T. The dips in reflectivity are the lowest three polariton branches. The red dotted lines show the dispersion of the lowest two exciton states for these values of the fields, and the blue dashed line is the bare cavity mode. Anticrossings of a few meV are typical for the strong-coupling regime.

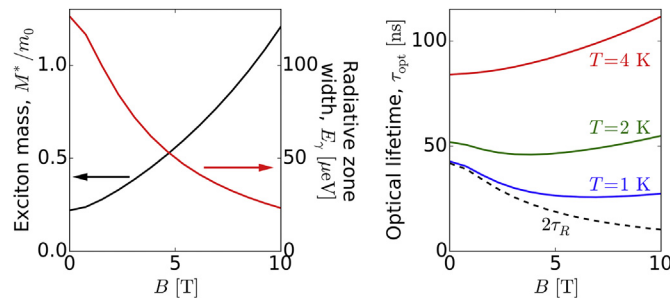


Fig. 5. (a) Effective mass M^* and radiative zone width E_γ of the ground state exciton as a function of magnetic field using $\epsilon_b = 12.1$, $\mu = 0.049m_0$ and $x = 0.11m_0$. All other parameters are the same as those used for Fig. 4. (b) Magnetic field dependence of the optical lifetime of an exciton gas at different temperatures calculated using (10) with $n_x = 5 \times 10^{10}$ cm $^{-2}$. The dashed line shows the radiative lifetime of a single exciton multiplied by two.

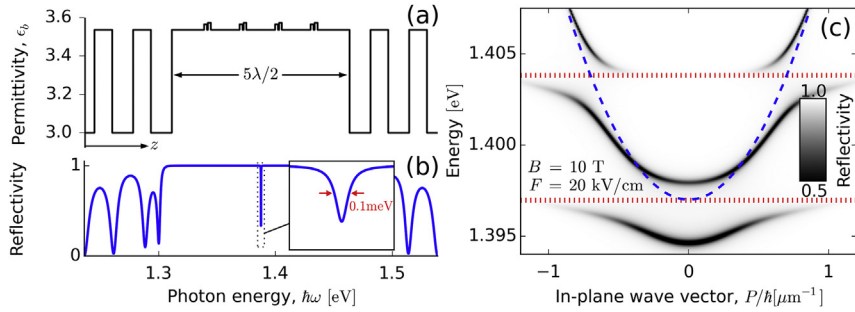


Fig. 6. (a) The spatial profile of the permittivity in the considered sample, having four pairs of InGaAs QWs located at the antinode positions of the resonant cavity mode in a $5\lambda/2$ cavity surrounded by two DBRs formed from 17 and 21 pairs of GaAs/InGaAs layers. (b) Reflectivity spectrum of the cavity in the absence of light-matter coupling. The inset shows a magnification of the cavity mode. (c) In-plane wave vector dependence of the reflectivity spectrum. The bare cavity mode and the exciton dispersion are shown by the dashed blue and dotted red lines, respectively.

4.2. Field dependence of the polariton reflectivity spectrum

The electric field dependence of the reflectivity spectrum of dipolaritons in a 10 T magnetic field is shown by the grayscale in Fig. 7(a). The ground and first excited exciton states are shown by red circles. The circle areas are proportional to the exciton linewidth. The plot is focussed on the anticrossing between the bright direct and dark indirect excitons. Dipolaritons are realized when the cavity mode (shown by the blue dashed line) is close in energy to one of the exciton branches. Lines of minimum reflectivity are the polariton branches, the lowest three of which are labelled. Polariton state 3 is faint causing only a small dip in reflectivity and its energy closely follows the first excited state of the exciton. Similarly, for $F < 20$ kV/cm, state 2 closely follows the exciton ground state and is not very visible.

Note that while treating polaritons on the microscopic level, we do not address the quantized polariton eigenstates directly but approach them as features in the response functions of a continuous wave excitation (particularly, the minima of the reflectivity). One can instead treat (11) directly as an eigenvalue problem, by imposing outgoing wave boundary conditions to the electric field and finding the polariton eigenstates. In both cases, the full interplay of the exciton COM and relative motion is taken into account microscopically. This leads to a richer dependence of the optical spectra on external fields [27,28] compared to some simpler approaches, such as a three-level polariton model consisting of only mixed direct, indirect exciton, and cavity mode states [12]. The latter approach actually neglects the exciton internal structure, treating it as a point-like object which results in an artefact of a fully dark polariton state.

4.3. Brightness and dipole moment of the polariton branches

We define the brightness of polariton states as their oscillator strength which in turn determine the strength of the light-matter coupling. This is calculated from the electron-hole overlap integral using a polariton wave function given by the microscopic exciton polarization (see Ref. [28] for full details of the calculation). Fig. 8(a) shows the brightness as a function of F for a fixed B for the lowest 3 polariton branches indicated in Fig. 7(a). The polariton dipole moment, $\langle z_e - z_h \rangle$ is shown in Fig. 8(c). Comparing with Fig. 8(a), an anticorrelation between the brightness and dipole moment is seen. This is expected as an increase in dipole moment comes at the cost of reducing the overlap of electron and hole wave functions. Decreasing the

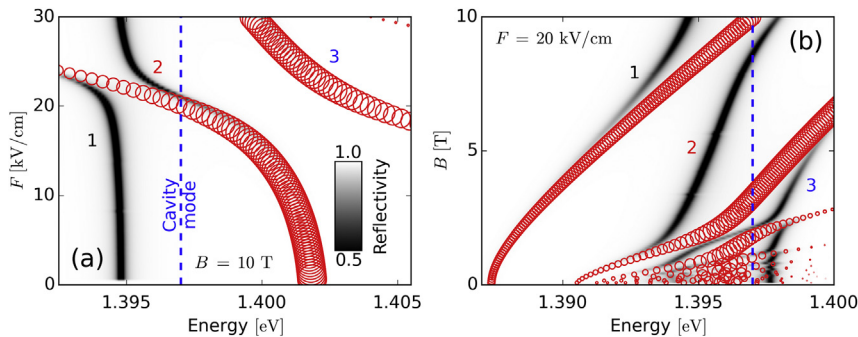


Fig. 7. Polariton reflectivity spectrum (grayscale) for (a) the electric field dependence with $B = 10$ T and (b) the magnetic field dependence with $F = 20$ kV/cm. Exciton states are shown by circles with area proportional to the oscillator strength. The cavity mode is shown by the blue dashed line. The lowest three polariton states are labelled.

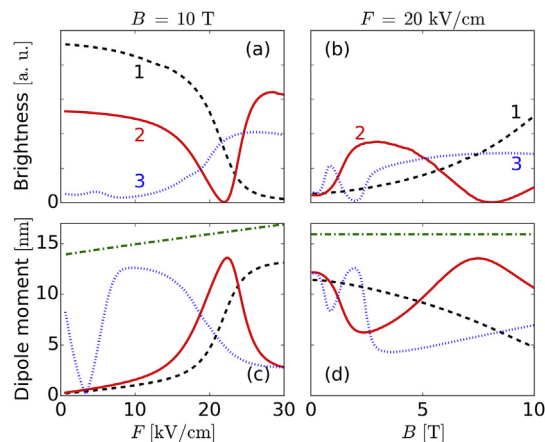


Fig. 8. Brightness (a,b) and static dipole moment (c,d) of the lowest three polariton states as a function of F with $B = 10$ T (a,c) and as a function of B with $F = 20$ kV/cm (b,d). The states in (a,c) and (b,d) correspond to those labelled in Fig. 7(a) and (b), respectively. The dash-dotted lines in (c) and (d) are the maximum nominal dipole moment [27].

overlap integral darkens the exciton state thus causing a darkening of the polariton. The dipole moment is strongly correlated to the gradient of the exciton energy with respect to electric field ($\partial E/\partial F \approx -e(z_e - z_h)$). This is particularly visible for states 1 and 2 when comparing Figs. 7(a) and 8(c).

Fig. 7(b) shows the same quantities as Fig. 7(a) but as a function of magnetic field with 20 kV/cm electric field. The corresponding brightness and dipole moment of the lowest three polariton branches are shown in Fig. 8(b) and (d). Oscillations in the brightness and dipole moment originate from the many anticrossings between different exciton states. Each anticrossing perturbs $\partial E/\partial F$ and, in turn, the dipole moment.

5. Summary

The paper presents the general multi-sub-level approach (MSLA) for calculating the properties of excitons and polaritons in microcavity embedded semiconductor planar heterostructures. The approach was used to calculate exciton states in semiconductor CQWs with electric and magnetic fields applied perpendicular to the QW plane. From the energies and wave functions of such states we extract the absorption spectrum, Bohr radius, dipole moment, binding energy, optical lifetime and magnetic field induced effective mass enhancement. The MSLA describes the electric field driven direct-indirect exciton crossover. This is characterized by increasing exciton radius, dipole moment and lifetime and decreasing binding energy. The optical lifetime of an exciton fluid was calculated by considering the occupation of optically active states that sit within the light cone. We showed that this factor leads to a lifetime that increases with increasing magnetic field. This is in contrast to the radiative lifetime of a single-exciton which decreases with increasing magnetic field due to a shrinkage of the in-plane Bohr radius. Exciton wave functions calculated via the MSLA were used to describe polaritons formed when CQWs are embedded in an optical microcavity at the antinode position of a resonant cavity mode. This approach offers a thorough description of the internal structure of a polariton. We demonstrated electric and magnetic field control of the dipolariton brightness and dipole moment. The properties of excitons and polaritons calculated here are important for modelling their respective fluids.

Acknowledgements

Support of this work by the EPSRC (Grant No. EP/L022990/1) is gratefully acknowledged. Computational work was done using the facilities of the ARCCA Division, Cardiff University. E.A.M. acknowledges support by RBRF (Grant No. 16-29-03333 ofi-m). Information on the data that underpins the results presented in this article, including how to access them, can be found in Cardiff University's data catalogue at <http://doi.org/10.17035/d.2017.0031596697>.

References

- [1] A.A. High, J.R. Leonard, M. Remeika, L.V. Butov, M. Hanson, A.C. Gossard, *Nano Lett.* 12 (2012) 2605.
- [2] K.B. Davis, M.O. Mewes, M.R. Andrews, N.J. van Druten, D.S. Durfee, D.M. Kurn, W. Ketterle, *Phys. Rev. Lett.* 75 (1995) 3969.
- [3] Y. Shilo, K. Cohen, B. Laikhtman, R. Rapaport, K. West, L. Pfeiffer, *Nat. Commun.* 4 (2013) 2335.
- [4] A.T. Hammack, L.V. Butov, J. Wilkes, L. Mouchliadis, E.A. Muljarov, A.L. Ivanov, A.C. Gossard, *Phys. Rev. B* 80 (2009) 155331.
- [5] A.G. Winbow, J.R. Leonard, M. Remeika, Y.Y. Kuznetsova, A.A. High, A.T. Hammack, L.V. Butov, J. Wilkes, A.A. Guenther, A.L. Ivanov, M. Hanson, A.C. Gossard, *Phys. Rev. Lett.* 106 (2011) 196806.
- [6] J.R. Leonard, M. Remeika, M.K. Chu, Y.Y. Kuznetsova, A.A. High, L.V. Butov, J. Wilkes, M. Hanson, A.C. Gossard, *Appl. Phys. Lett.* 100 (2012) 231106.
- [7] C.J. Dorow, Y.Y. Kuznetsova, J.R. Leonard, M.K. Chu, L.V. Butov, J. Wilkes, M. Hanson, A.C. Gossard, *Appl. Phys. Lett.* 108 (2016) 073502.

- [8] P. Andreakou, S.V. Poltavtsev, J.R. Leonard, E.V. Calman, M. Remeika, Y.Y. Kuznetsova, L.V. Butov, J. Wilkes, M. Hanson, A.C. Gossard, *Appl. Phys. Lett.* 104 (2014) 091101.
- [9] J. Kasprzak, M. Richard, S. Kundermann, A. Baas, P. Jeambrun, J.M.J. Keeling, F.M. Marchetti, M.H. Szymanska, R. Andre, J.L. Staehli, V. Savona, P.B. Littlewood, B. Deveaud, L.S. Dang, *Nature* 443 (2006) 409.
- [10] A. Amo, D. Sanvitto, F.P. Laussy, D. Ballarini, E.d. Valle, M.D. Martin, A. Lemaître, J. Bloch, D.N. Krizhanovskii, M.S. Skolnick, C. Tejedor, L. Vina, *Nature* 457 (2009) 291.
- [11] K.G. Lagoudakis, M. Wouters, M. Richard, A. Baas, I. Carusotto, R. Andre, L.S. Dang, B. Deveaud-Pledran, *Nat. Phys.* 4 (2008) 706.
- [12] P. Cristofolini, G. Christmann, S.I. Tsintzos, G. Deligeorgis, G. Konstantinidis, Z. Hatzopoulos, P.G. Savvidis, J.J. Baumberg, *Science* 336 (2012) 704.
- [13] I. Rosenberg, Y. Mazuz-Harpaz, R. Rapaport, K. West, L. Pfeiffer, *Phys. Rev. B* 93 (2016) 195151.
- [14] C.G.M. Steger, D.W. Snoke, L. Pfeiffer, K. West, *Optica* 2 (2015) 1.
- [15] O. Kyriienko, A.V. Kavokin, I.A. Shelykh, *Phys. Rev. Lett.* 111 (2013) 176401.
- [16] J. Li, S. Duan, W. Zhang, *Europhys. Lett.* 108 (2014) 67010.
- [17] O. Kyriienko, I.A. Shelykh, T.C.H. Liew, *Phys. Rev. A* 90 (2014) 033807.
- [18] P.I. Khadzhi, O.F. Vasilieva, *JETP Lett.* 102 (2015) 665.
- [19] O. Kyriienko, T.C.H. Liew, *Phys. Rev. B* 93 (2016) 035301.
- [20] V. Shahnazaryan, O. Kyriienko, I.A. Shelykh, *Phys. Rev. B* 91 (2015) 085302.
- [21] N.K.J. Su, Y. Yamamoto, A.H. MacDonald, *Phys. Rev. Lett.* 112 (2014) 116401.
- [22] K. Sivalertporn, L. Mouchliadis, A.L. Ivanov, R. Philp, E.A. Muljarov, *Phys. Rev. B* 85 (2012) 045207.
- [23] P. Andreakou, A.V. Mikhailov, S. Cronenberger, D. Scalbert, A. Nalitov, A.V. Kavokin, M. Nawrocki, L.V. Butov, K.L. Campman, A.C. Gossard, M. Vladimirova, *Phys. Rev. B* 93 (2016) 115410.
- [24] K. Sivalertporn, *Phys. Lett. A* 380 (2016) 1990.
- [25] J. Wilkes, E.A. Muljarov, *New J. Phys.* 18 (2016) 023032.
- [26] D. Ko, J.C. Inkson, *Phys. Rev. B* 38 (1988) 9945.
- [27] K. Sivalertporn, E.A. Muljarov, *Phys. Rev. Lett.* 115 (2015) 077401.
- [28] J. Wilkes, E.A. Muljarov, *Phys. Rev. B* 94 (2016) 125310.
- [29] L.P. Gor'kov, I.E. Dzyaloshinskii, *JETP* 26 (1968) 449.
- [30] Yu E. Lozovik, A.M. Ruvinskii, *JETP* 85 (1997) 979.
- [31] Yu. E. Lozovik, I.V. Ovchinnikov, S. Yu. Volkov, L.V. Butov, D.S. Chemla, *Phys. Rev. B* 65 (2002) 235304.
- [32] L.V. Butov, A.C. Gossard, D.S. Chemla, *Nature* 418 (2002) 751.
- [33] M. Alloing, A. Lemaître, E. Galopin, F. Dubin, *Sci. Rep.* 3 (2013) 1587.
- [34] A. Gärtner, A.W. Holleitner, J.P. Kotthaus, D. Schuh, *Appl. Phys. Lett.* 89 (2006) 052108.
- [35] P.I. Arseev, A.B. Dzyubenko, *JETP* 87 (1998) 200.
- [36] L.V. Butov, A.A. Shashkin, V.T. Dolgoplov, K.L. Campman, A.C. Gossard, *Phys. Rev. B* 60 (1999) 8753.
- [37] L.C. Andreani, *Solid State Commun.* 77 (1991) 641.
- [38] Y. Y. Kuznetsova, C. J. Dorow, E. V. Calman, L. V. Butov, J. Wilkes, K. L. Campman and A. C. Gossard, (preprint) arXiv:1610.03116 (2016).
- [39] A. Stahl, I. Balslev, *Electrodynamics of the Semiconductor Band Edge*, Springer-Verlag, Berlin, 1987.
- [40] Y. Sun, P. Wen, Y. Yoon, G. Liu, M. Steger, L.N. Pfeiffer, K. West, D.W. Snoke, K.A. Nelson, *Phys. Rev. Lett.* 118 (2017) 016602.